



## Facile homogeneous precipitation method to prepare MnO<sub>2</sub> with high performance in catalytic oxidation of ethyl acetate

Tingting Pan<sup>a,b</sup>, Hua Deng<sup>a,b,\*</sup>, Shunyu Kang<sup>a</sup>, Yan Zhang<sup>a</sup>, Wang Lian<sup>c</sup>, Changbin Zhang<sup>c</sup>, Hong He<sup>a,b,c</sup>

<sup>a</sup> Center for Excellence in Regional Atmospheric Environment, Key Laboratory of Urban Pollutant Conversion, Institute of Urban Environment, Chinese Academy of Sciences, Xiamen 361021, China

<sup>b</sup> University of Chinese Academy of Sciences, Beijing 100049, China

<sup>c</sup> Research Center for Eco-Environmental Sciences, Chinese Academy of Sciences, Beijing 100085, China

### ARTICLE INFO

#### Keywords:

Catalytic oxidation  
Volatile organic compound  
α-MnO<sub>2</sub>  
Homogeneous precipitation method  
Ethyl acetate

### ABSTRACT

A facile homogeneous precipitation method driven by synchronous reactions of urea hydrolysis and potassium permanganate reduction is proposed for preparation of MnO<sub>2</sub> catalysts. Pure α-MnO<sub>2</sub> nanostructures with different morphologies, including nanowires, nanorods and nanoparticles, were obtained by simply tuning the precipitation conditions. The evolution of materials derived from different preparation conditions was investigated via X-ray diffraction, transmission electron microscopy, N<sub>2</sub> adsorption, X-ray photoelectron spectroscopy, chemisorption and DFT calculations. The precipitation temperature and time significantly influenced the physicochemical properties of as-prepared catalysts. With increasing precipitation temperature and time, the degree of crystallinity, BET surface area and amount of surface-adsorbed oxygen of α-MnO<sub>2</sub> exhibited a substantial increase. The main exposed surface facets varied from (2 0 0), (3 1 0) to (2 1 1) as temperature and time increased. The best precipitation temperature and time were 90 °C and 24 h respectively. The optimal α-MnO<sub>2</sub> catalyst demonstrated 100% conversion of 1000 ppm ethyl acetate under the high space velocity of 78,000 h<sup>-1</sup> during a 113-h test at 190 °C, outperforming other manganese oxide catalysts and many typical noble metal catalysts in terms of activity and stability. Experimental results and DFT calculations were consistent and indicated that surface oxygen species originating from the (2 1 1) surface of α-MnO<sub>2</sub> were most active. This study provides important insights for manipulating the morphology of MnO<sub>2</sub> by a facile method and remarkably promoting the performance for ethyl acetate VOC elimination.

### 1. Introduction

The increasing emissions of volatile organic compounds (VOCs) linked with industrialization and urbanization severely threaten the ecological environment [1–3]. For instance, anthropogenic NMVOC emissions in China increased from 9.76 Tg in 1990 to 28.5 Tg in 2017 [4]. These vast VOCs emissions contribute to heavy haze and the formation of tropospheric ozone (O<sub>3</sub>), which endanger human health. Catalytic oxidation is considered as one of the most feasible technologies for the removal of VOCs in comparison with other treatments (adsorption, plasma catalysis, photocatalytic oxidation, etc.) [3], due to its high efficiency, energy savings, and environmental friendliness. The catalysts for VOC oxidation include noble metals [5–11] and transition metal oxides [12–15]. The noble metal catalysts such as Pt- and Pd-based

materials are the most efficient catalysts for total oxidation of VOCs, but with the disadvantages of low natural abundance and high cost. The development of noble-metal-free metal oxides and eco-catalysts operating at low-temperatures is highly desirable.

Among these catalysts, manganese-based catalysts, including spinel-type [16,17], binary oxides [18,19] and mixed-metal oxides [20,21] are highly efficient and economical catalysts for VOC oxidation. Among them, MnO<sub>2</sub> [21–24] has attracted more and more attention due to its superior redox properties. In nature, MnO<sub>2</sub> can form many kinds of polymorphs, such as the α-, β-, γ-, and δ- polytypes. The α-MnO<sub>2</sub> phase has drawn considerable attention for its good catalytic performance in the deep oxidation of VOCs because of its abundant lattice oxygen species and good reducibility [25–27]. To obtain α-MnO<sub>2</sub> catalysts with excellent catalytic performance in terms of activity and stability,

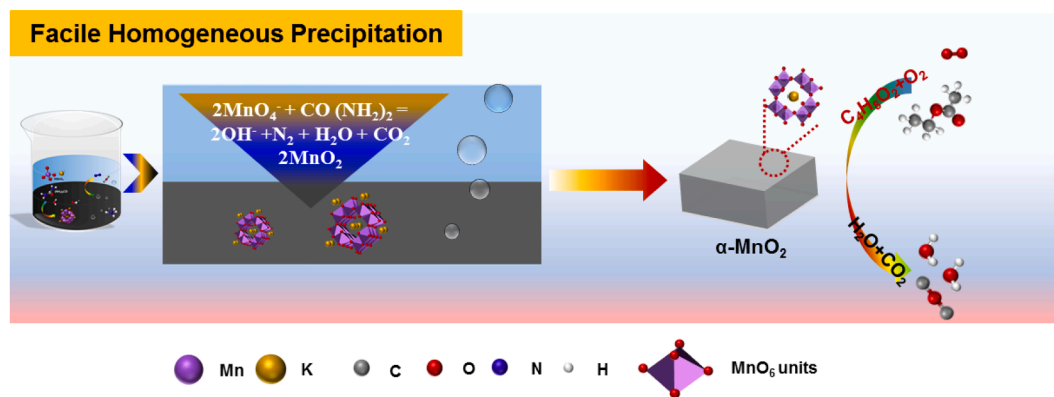
\* Corresponding author at: University of Chinese Academy of Sciences, Beijing 100049, China.  
E-mail address: [huadeng@iue.ac.cn](mailto:huadeng@iue.ac.cn) (H. Deng).

<https://doi.org/10.1016/j.cej.2021.129246>

Received 26 October 2020; Received in revised form 27 February 2021; Accepted 1 March 2021

Available online 11 March 2021

1385-8947/© 2021 Elsevier B.V. All rights reserved.



Scheme 1. Illustration of the homogeneous precipitation reaction.

numerous synthesis techniques have been developed, including the hydrothermal method, sol-gel method, co-precipitation method, etc.

The hydrothermal method has been the most common route to preparing MnO<sub>2</sub> materials [28–31]. However, it requires expensive equipment with high pressure resistance, and its high energy consumption limits large-scale application. The sol-gel method [32] does not depend on special reactors, but has poor atomic economy with easy loss of valuable components, which eventually cause solvent pollution [33]. The co-precipitation method is a facile method and appropriate for mass production [34]. However, some inactive heterogeneous components coexist inevitably in the as-prepared catalysts [35,36]. Homogeneous precipitation is optimal for co-precipitation synthesis, and massive amounts of products can be produced. Meanwhile, highly pure active phases [37] can be synthesized via tuning the preparation conditions. To the best of our knowledge, there are few reports on the development of nano  $\alpha$ -MnO<sub>2</sub> via facile homogeneous precipitation methods for application in VOC oxidation.

In order to synthesize  $\alpha$ -MnO<sub>2</sub> with good performance, some researchers have been successful in tuning the morphologies via reflux, solid-state reaction and hydrothermal methods [38–41]. Zhang et al [42] demonstrated that nanofiber-like  $\alpha$ -MnO<sub>2</sub> with more oxygen vacancies exhibits better activity than that of nanorod and nanotube  $\alpha$ -MnO<sub>2</sub>. Li et al [43] manipulated the oxygen vacancy density of  $\alpha$ -MnO<sub>2</sub> with nanorod morphology, which demonstrated excellent removal efficiency for benzene. Actually, different exposed facets exhibited various surface coordination environments, which determined the properties of oxygen defects [44]. For instance, Rong et al [45] reported that  $\alpha$ -MnO<sub>2</sub> (3 1 0) facets possess more oxygen vacancies than (1 1 0) and (1 0 0) facets. Jia et al [42] found that the atomic configuration of  $\alpha$ -MnO<sub>2</sub> (2 1 1) facets contains more unsaturated manganese, which is favorable to the formation of more oxygen vacancies. These results indicate that tuning the morphologies and crystal facets are effective means to improve the catalytic oxidation activity of MnO<sub>2</sub>. However, few literatures are successful in synthesis of high index crystal faces such as (2 1 1) faces.

In this study, a facile homogeneous precipitation method is introduced. Different morphologies were obtained, including nanowires, nanorods and nano-particles, which exposed different dominant high index facets, such as (2 1 1), (3 1 0) and (2 0 0) crystal planes. The nanoparticulate  $\alpha$ -MnO<sub>2</sub> exhibited high stability and the best activity ever achieved in the oxidation of ethyl acetate, which is considered one of the most difficult molecules to oxidize [46]. Numerous characterization methods were applied to reveal the relationship between structure and activity. The highly reactive (2 1 1) plane contributed to the best activity of the nano-particulate  $\alpha$ -MnO<sub>2</sub>. With the aid of DFT calculation, the surface oxygen species originating from different exposed surfaces were compared, among which oxygen species derived from the high index (2 1 1) surface of  $\alpha$ -MnO<sub>2</sub> were found to be most active in VOC oxidation.

## 2. Experimental section

### 2.1. Illustration of the homogeneous precipitation process

We herein describe a chemical route to uniformly introduce NH<sub>4</sub><sup>+</sup> into a KMnO<sub>4</sub> solution, in which the formed NH<sub>4</sub>MnO<sub>4</sub> tends to decompose easily as follows: 2NH<sub>4</sub>MnO<sub>4</sub> (s) = N<sub>2</sub> (g) + 2MnO<sub>2</sub> (s) + 4H<sub>2</sub>O (l). The homogeneous precipitation proceeds by consumption of NH<sub>4</sub><sup>+</sup> ions. In fact, NH<sub>4</sub><sup>+</sup> ions can be released slowly by the following reactions: CO (NH<sub>2</sub>)<sub>2</sub> (s) + H<sub>2</sub>O (l)  $\xrightarrow{>70^\circ\text{C}}$  CO<sub>2</sub> (g) + 2NH<sub>3</sub> (g), NH<sub>3</sub> (g) + H<sub>2</sub>O (l)  $\rightleftharpoons$  NH<sub>4</sub><sup>+</sup> (aq) + OH<sup>-</sup> (aq) ( $\Delta G = -210.16$  kJ/mol) [47]. The combined reactions lead to a spontaneous reaction as follows: 2MnO<sub>4</sub><sup>-</sup> (aq) + CO (NH<sub>2</sub>)<sub>2</sub> (l) = N<sub>2</sub> (g) + 2MnO<sub>2</sub> (s) + H<sub>2</sub>O (l) + 2OH<sup>-</sup> + CO<sub>2</sub> ( $\Delta G = -647.56$  kJ/mol). The properties of the products are influenced by a combination of several factors, including hydrolysis temperature, precipitation time and calcination temperature, all of which were carefully examined. As stated above, a homogenous MnO<sub>2</sub> catalyst could be obtained during synchronous MnO<sub>2</sub> precipitation and NH<sub>3</sub> hydrolysis reactions, which are illustrated in Scheme 1.

### 2.2. Catalyst preparation

The  $\alpha$ -MnO<sub>2</sub> catalysts were prepared by the homogeneous precipitation method. In a typical synthesis, 0.3 mol KMnO<sub>4</sub> (XiLONG SCIENTIFIC) as the Mn precursor was firstly dissolved in 372 mL deionized water under stirring to form a solution. An excess of urea (Sinopharm Chemical Reagent) to precipitate all precursors was then added into the solution. The solution was magnetically stirred at room temperature for 3 h, then heated to 90 °C with a plastic film cover and held there for 24 h under vigorous stirring. After filtering, washing and drying at 100 °C overnight, the solids were calcined at 500 °C for 3 h in a muffle furnace with a heating rate of 5 °C/min to obtain the final products. In order to determine the optimal preparation conditions, we also prepared  $\alpha$ -MnO<sub>2</sub> with different water bath times, water bath temperatures and calcination temperatures. First, we evaluated the effect of the reaction temperature (Y °C) on the catalytic activity of the corresponding  $\alpha$ -MnO<sub>2</sub> catalysts (MnO<sub>2</sub>-Y, Y = 70, 80 and 90), with the water bath time set to 24 h. Next, we varied the reaction time (X h) of the water bath to obtain a series of  $\alpha$ -MnO<sub>2</sub> catalysts (MnO<sub>2</sub>-Xh, X = 6, 12, 24, 48) at the optimum temperature. The calcination temperature was also considered, and controlled from 400 °C to 600 °C in intervals of 100 °C, setting the previous two parameters at 24 h and 90 °C. The weights of  $\alpha$ -MnO<sub>2</sub> products were recorded after different preparations as shown in Table S1. One of the most attractive advantages of the homogeneous co-precipitation method is that the utilization of the Mn source is relatively high as to 100%. According to the yield rate calculation, all Mn ions were effectively embedded into the lattice of  $\alpha$ -MnO<sub>2</sub> under suitable conditions.

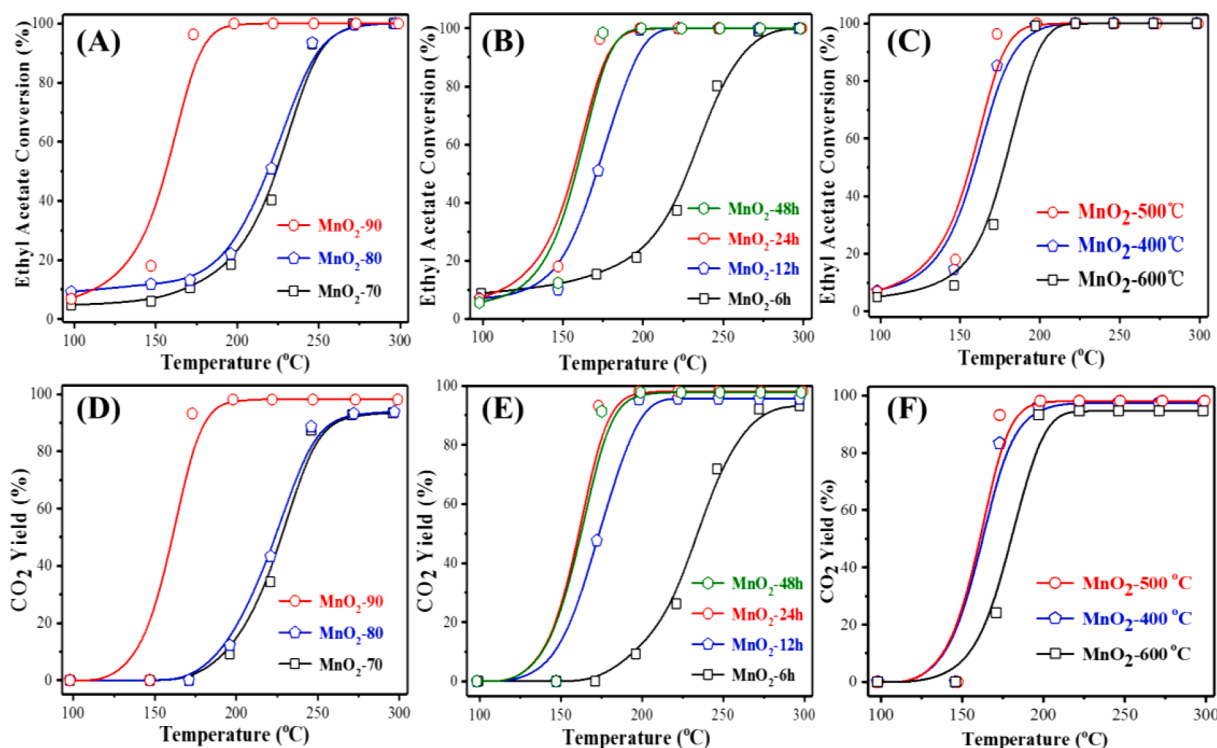


**Fig. 1.** Catalytic activities of  $\alpha$ -MnO<sub>2</sub> prepared with various precipitation temperatures (A, D), precipitation periods (B, E) and calcination temperatures (C, F). Reaction conditions: [Ethyl Acetate] = 1000 ppm, [O<sub>2</sub>] = 20 vol%, GHSV = 78000 h<sup>-1</sup>.

### 2.3. Catalyst characterization

The X-ray powder diffraction patterns of the catalysts were recorded by an X'Pert Pro XRD diffractometer (PANalytical B.V., Netherlands) with Cu K $\alpha$  radiation ( $\lambda = 1.5406 \text{ \AA}$ ) at 40 kV and 40 mA. The morphology of catalysts was characterized by a Hitachi S-4800 field emission scanning electron microscope (FE-SEM). HRTEM was employed using a JEOL 2100F instrument, with the Cs calibration probe operated under 200 kV. N<sub>2</sub> physisorption analysis was carried out at 77 K using an ASAP 2020 N autoscore surface analyzer. The specific surface area and pore volume were calculated by the Brunauer–Emmett–Teller (BET) method. X-ray photoelectron spectra (XPS) were measured on an ESCALAB250 spectrometer using monochromatic Al K $\alpha$  as the X-ray source (1486.6 eV). The adventitious C 1 s peak at 284.6 eV was utilized for calibration of the binding energies (BEs) of all the elements. Elemental analysis was conducted using an inductively coupled plasma emission spectrometer (ICP-OES, Agilent 700). All samples were dissolved using strong acid solution before testing. The continuum spectra of the samples were fitted in accordance with Gaussian-Lorentzian line shapes. H<sub>2</sub> temperature-programmed reduction (H<sub>2</sub>-TPR) experiments were conducted on a Micromeritics Auto chem II 2920 adsorption instrument. The sample (60 mg) was pretreated at 150 °C for 1 h before measurement. After cooling to 30 °C, it was reduced in a 50 mL·min<sup>-1</sup> flowing gas mixture of 5 vol% H<sub>2</sub> and Ar while being gradually heated to 700 °C. The variation in H<sub>2</sub> concentration was monitored with a thermal conductivity detector (TCD). In situ diffuse reflectance infrared Fourier transform spectra (in situ DRIFTS) were recorded on a Thermo Fisher IS50 FTIR spectrometer, equipped with an in situ diffuse reflectance chamber (Harrick) and high sensitivity MCT/A detector. The detailed test steps are described in [Text S1](#).

### 2.4. Catalytic evaluation

The complete oxidation of ethyl acetate was performed in a fixed-bed continuous flow quartz reactor (8 mm i.d.), in which 0.2 g catalyst

(40–60 mesh) was loaded and held in place by quartz wool. The reactant mixture was composed of 1000 ppm ethyl acetate, 20 vol% O<sub>2</sub> in N<sub>2</sub> balance at a total flow rate of 300 mL/min, giving a gaseous hourly space velocity (GHSV) of 78,000 h<sup>-1</sup> (SV = 120,000 mL/(g·h)). The ethyl acetate vapor was produced by passing N<sub>2</sub> through a bottle containing pure ethyl acetate (A.R.), which was chilled in an isothermal bath of ice water. To minimize the adsorption of ethyl acetate on tube walls, all gas lines were kept at 80 °C. The VOC (ethyl acetate) concentration was analyzed online by a gas chromatograph (GC; Agilent 7890B, HP-5 capillary column) with a flame ionization detector. CO, CO<sub>2</sub> and O<sub>2</sub> concentrations were analyzed by the same GC with another inlet channel, which was equipped with a flame ionization detector and a thermal conductivity detector (Porapak Q and HayeSep Q columns). The column oven was kept at 80 °C to separate all components. In all the experiments, ethyl acetate conversion was calculated using the following equation:

$$\text{EthylAcetateConversion}(\%) = \left(1 - \frac{[\text{EthylAcetate}]_{\text{out}}}{[\text{EthylAcetate}]_{\text{in}}}\right) \times 100\%$$

The CO<sub>2</sub> yield was defined as follows:

$$\text{CO}_2\text{Yield}(\%) = \frac{[\text{CO}_2]_{\text{out}}}{[\text{EthylAcetate}]_{\text{in}} \times 4} \times 100\%$$

### 2.5. DFT calculation

Periodic DFT calculations were performed using the plane-wave method (the Vienna Ab-initio Simulation Package). The exchange–correlation functional was treated within the GGA approximation parameterized by PBE. The electron–ion interaction was described by the projector augmented wave (PAW) approach. The inter-slab distance was maintained at 15 Å to avoid inter-slab interactions in the periodic system. A tight convergence of the plane-wave expansion was obtained with a kinetics energy cut-off of 400 eV. The electron configurations 2s<sup>2</sup>2p<sup>4</sup>, 3d<sup>5</sup>4s<sup>2</sup>, 3p<sup>6</sup>4s<sup>1</sup> were considered for the valence electrons of O,

**Table 1**

Comparison of ethyl acetate oxidation catalysts known to exhibit good performance.

Catalysts	Ethyl acetate concentration(ppm)	GHSV( $\text{h}^{-1}$ )	$T_{90}$ ( $^{\circ}\text{C}$ )	References
Ce-Ni	466.7	53,050	230	[51]
Fe-Ti	1.21 mol%	100	397	[52]
Co/CeO <sub>2</sub>	466.7	60,000	260	[53]
Cu-Ce/SiO <sub>2</sub>	1.21 mol%	300	297	[54]
CuO/ZSM-5	1,500	15,000	235	[55]
Cu <sub>10</sub> /Al <sub>2</sub> O <sub>3</sub> -MnO <sub>x</sub> -CeO <sub>2</sub>	1802 mg/m <sup>3</sup>	5,000	300	[56]
Pt-TiO <sub>2</sub> /Ti	1,000	60,000 mL g <sup>-1</sup> h <sup>-1</sup>	205	[20]
Pt-Ti-Al/Al <sub>2</sub> O <sub>3</sub>	1,000	2,000	290	[46]
Pd/CCY-500	1,000	10,000	300	[57]
Pd/Al <sub>2</sub> O <sub>3</sub>	1,000	—	260	[58]
α-MnO <sub>2</sub>	1,000	78,000	278	This work
	1,000	78,000	176	This work

Mn and K respectively. The optimized pristine crystal lattice parameters of α-MnO<sub>2</sub> (KMn<sub>8</sub>O<sub>16</sub>) were as follows:  $a = b = 9.71 \text{ \AA}$ ,  $c = 2.85 \text{ \AA}$ , and  $\alpha = \beta = \gamma = 90$ , which is close to the values in many other reports [48–50]. Spin polarization was considered in all calculations. The convergence criteria for the electronic and ionic relaxation were  $10^{-5} \text{ eV}$  and  $0.02 \text{ eV \AA}^{-1}$ , respectively.

In order to evaluate the reactivity of surface oxygen species stemming from different exposed surfaces, three different surfaces (2 0 0), (3 1 0) and (2 1 1) were established on the basis of the former optimized model of α-MnO<sub>2</sub>. The energy for the removal of surface oxygen (oxygen vacancy formation energy) was calculated as follows:

$$E_{VO} = E_{def} - E_{bulk} + 1/2E_{O_2}$$

where  $E_{def}$  is the total energy of the model with loss of one surface oxygen,  $E_{bulk}$  is the total energy of the intact system and  $E_{O_2}$  is the energy of an O<sub>2</sub> molecule. Lower  $E_{VO}$  values indicate that the corresponding surface oxygen species is more active.

### 3. Results and discussion

#### 3.1. Catalytic performance

##### 3.1.1. Activity measurement

The catalytic activities of all materials for the total oxidation of ethyl acetate were evaluated to determine the optimal preparation parameters. Fig. 1(A) shows that precipitation temperature is a vital factor influencing the catalytic performance of the prepared MnO<sub>x</sub>. The oxidation of ethyl acetate with MnO<sub>2</sub>-90 as catalyst was much better than that with MnO<sub>2</sub>-80 and MnO<sub>2</sub>-70. As can be seen in Fig. 1(B), the precipitation time also significantly affected the catalytic activity of relevant samples. The ethyl acetate removal efficiency increased with increasing crystallization time. Since the activity of MnO<sub>2</sub>-24 h was similar to that of MnO<sub>2</sub>-48 h, the optimal bath time was fixed at 24 h to save energy. Three different calcination temperatures (400 °C, 500 °C and 600 °C) were also investigated as shown in Fig. 1(C). The sample without calcination was also characterized and tested as shown in Fig. S1. Activation of materials by calcination is indispensable because the un-calcined sample was in an amorphous form and the catalytic activity was very unstable. The activity sequence for different activation temperatures was as follows: 500 °C > 400 °C > 600 °C ≫ un-calcined. Considering both the activity and thermal stability, 500 °C was the best activation temperature. Actually, a much wider range of preparation parameters, including precipitation temperature (70, 80, 90, and 100 °C), precipitation time (6, 12, 24, 36, 48 h) and calcination temperature (300, 400, 500, 600 °C) were compared, with the results

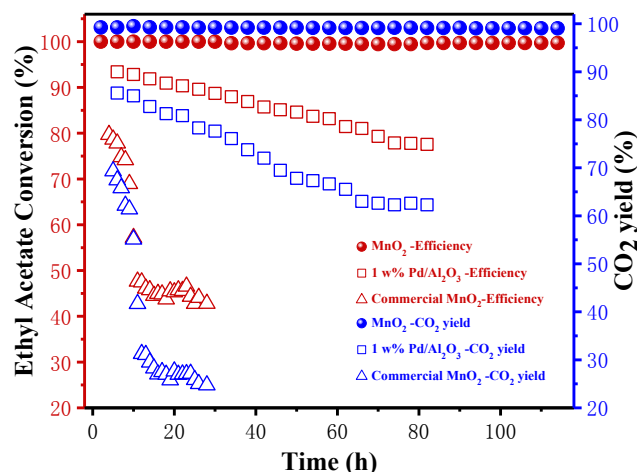


**Fig. 2.** Comparison of ethyl acetate conversion levels among α-MnO<sub>2</sub> (test at 190 °C), commercial MnO<sub>2</sub> (test at 190 °C) and 1 wt% Pd/Al<sub>2</sub>O<sub>3</sub> (test at 280 °C). Reaction conditions: [ethyl acetate] = 1000 ppm, [O<sub>2</sub>] = 20 vol%, GHSV = 78,000 h<sup>-1</sup>.

illustrated in Fig. S2-S5 and Text S2. On the basis of activity tests, the optimal precipitation temperature, time and thermal activation temperature were confirmed as 90 °C, 24 h, and 500 °C, respectively.

The as-obtained catalyst exhibited excellent activity in the oxidation of ethyl acetate. The  $T_{50}$  and  $T_{90}$  (corresponding to the respective reaction temperatures at which 50% and 90% of ethyl acetate conversion could be obtained) value was 150 °C and 176 °C respectively. The corresponding CO<sub>2</sub> yield profile was almost the same as the ethyl acetate conversion (Fig. 1(D)-(F)). It should be noted that the CO<sub>2</sub> yield of MnO<sub>2</sub>-70 and MnO<sub>2</sub>-80 in Fig. 1(D) is lower than the corresponding VOC conversion (Fig. 1(A)). The carbon balance was checked, with the results illustrated in Fig. S6. About 20% CO as byproduct decreased the CO<sub>2</sub> selectivity over MnO<sub>2</sub>-70 and MnO<sub>2</sub>-80, while MnO<sub>2</sub>-90 exhibited good CO<sub>2</sub> selectivity without noteworthy formation of the byproduct CO in the removal of ethyl acetate. A comparison between different catalysts known to exhibit good performance is shown in Table 1 and Table S2. It can be observed that our catalysts exhibited outstanding combined performance in terms of low-temperature activity and GHSV value compared to catalysts reported in the literature.

##### 3.1.2. Stability test

Catalytic stability is an important criterion for catalysts in industrial applications. Thus, a stability test was carried out over the selected α-MnO<sub>2</sub> catalyst. A noble metal catalyst (1 wt% Pd/Al<sub>2</sub>O<sub>3</sub>) prepared in our previous study [59] and a commercial MnO<sub>2</sub> catalyst (Sinopharm Chemical Reagent) were also applied in ethyl acetate oxidation for comparison. As shown in Fig. 2, during a 113-h test, the selected α-MnO<sub>2</sub> catalyst exhibited excellent stability, maintaining 100% ethyl acetate conversion and nearly 100% CO<sub>2</sub> yield. In contrast, the ethyl acetate conversion and CO<sub>2</sub> yield dropped sharply from 95% and 85% to 77.6% and 61.5% in 84 h, respectively, over Pd/Al<sub>2</sub>O<sub>3</sub>. The commercial MnO<sub>2</sub> catalyst exhibited the worst activity and stability in ethyl acetate oxidation, with the activity dropping to 45% in 28 h. The reason was further analyzed in Fig. S7, Table S3 and Text S3. The performance of the optimal α-MnO<sub>2</sub> catalyst in this work was far superior to that of Pd/Al<sub>2</sub>O<sub>3</sub> (Fig. S8) and commercial MnO<sub>2</sub>, demonstrating its promise as a catalyst for low-temperature catalytic oxidation of ethyl acetate. Since the homogeneous precipitation temperature and time influence the catalyst profoundly, both preparation parameters are addressed in the following discussion.

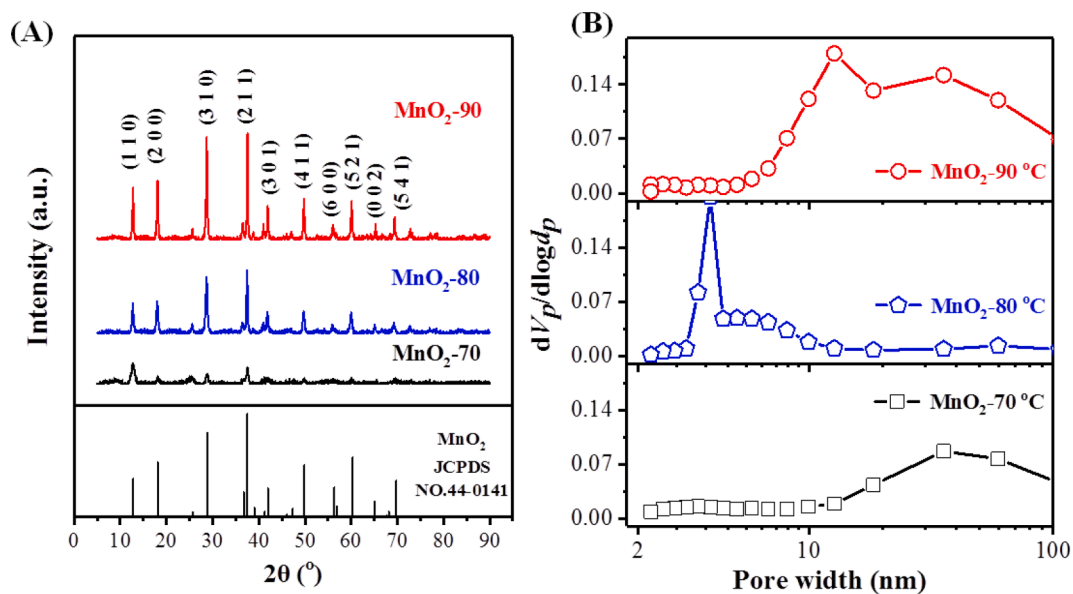


Fig. 3. Powder XRD pattern (A) and pore distribution (B) of MnO<sub>2</sub> catalysts prepared at different bath temperatures.

Table 2

XPS peak fitting parameters, atomic ratios and textural parameters of MnO<sub>2</sub> catalysts prepared at different precipitation temperatures.

Sample	Mn 2p			Mn 3s		O 1s			K/Mn		N <sub>2</sub> Physisorption	
	Mn <sup>3+</sup> (eV)	Mn <sup>4+</sup> (eV)	Mn <sup>4+</sup> /Mn <sup>3+</sup>	ΔEs	AOS	O <sub>latt</sub> (%)	O <sub>ads</sub> (%)	O <sub>ads</sub> /O <sub>latt</sub>	XPS	ICP	S <sub>BET</sub> (m <sup>2</sup> /g)	V <sub>m</sub> (mL/g)
MnO <sub>2</sub> -70	641.9	643.1	0.90	4.81	3.51	72.22	27.78	0.38	0.27	0.24	13.82	0.07
MnO <sub>2</sub> -80	641.8	642.9	0.95	4.76	3.57	73.24	26.76	0.37	0.21	0.16	16.93	0.04
MnO <sub>2</sub> -90	641.9	642.9	1.16	4.54	3.82	65.57	34.43	0.52	0.11	0.11	34.30	0.16

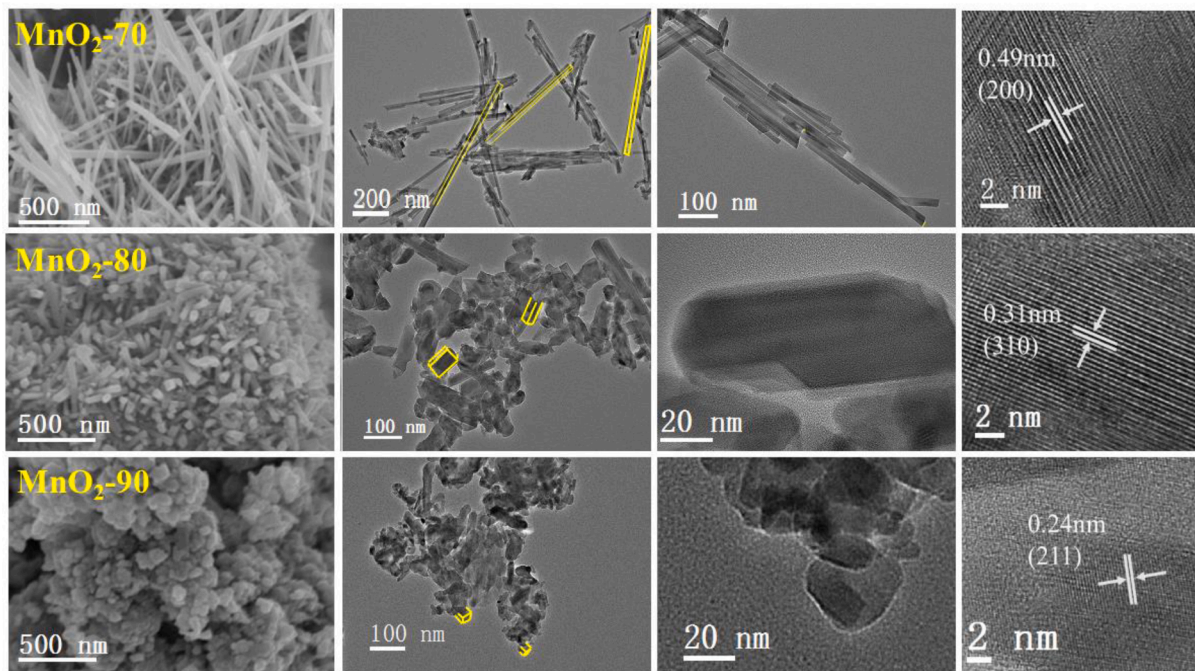


Fig. 4. Images showing the morphology of MnO<sub>2</sub>-70, MnO<sub>2</sub>-80, and MnO<sub>2</sub>-90.

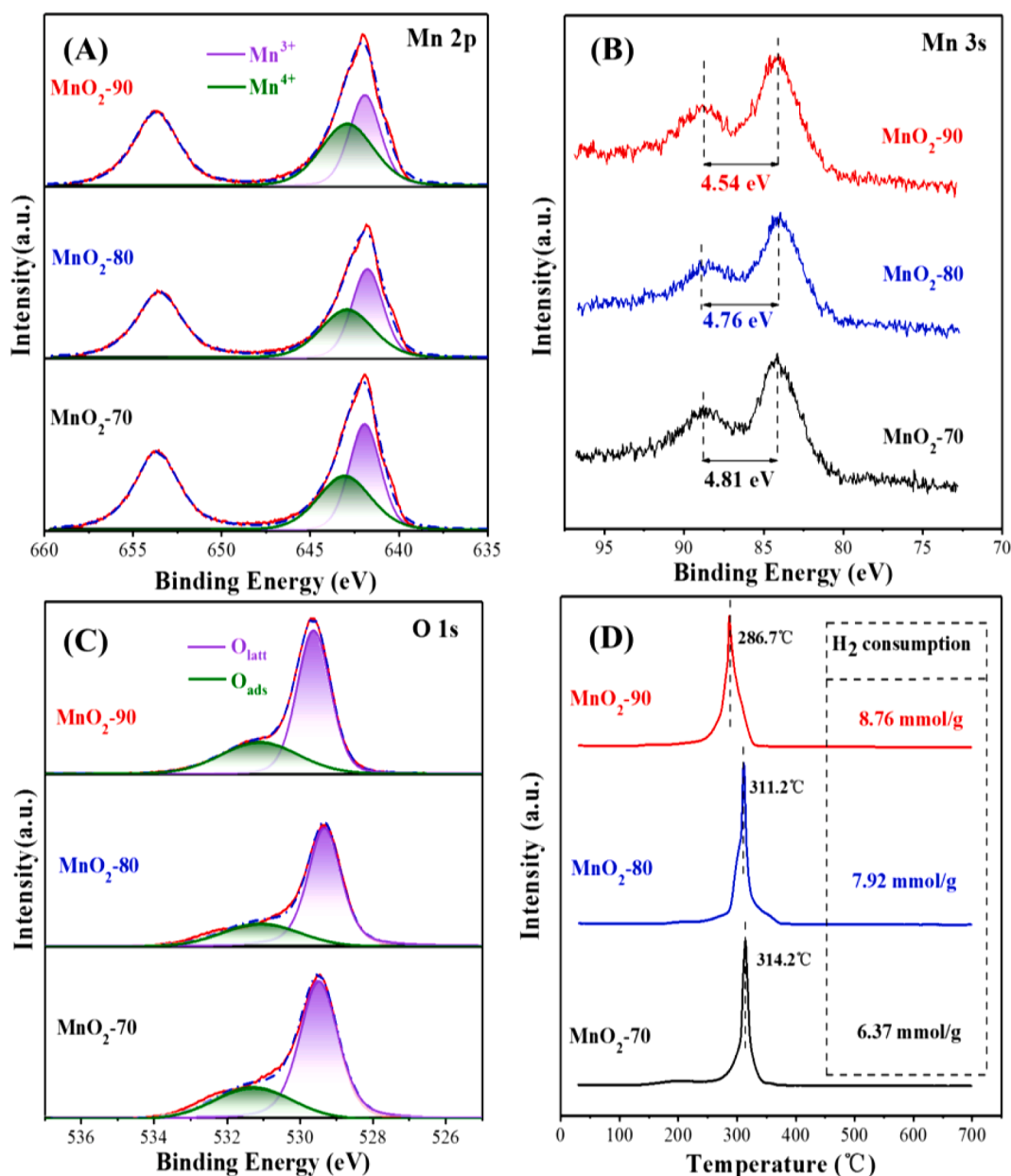


Fig. 5. XPS spectra of Mn 2p (A), Mn 3 s (B), O 1 s (C) regions, and H<sub>2</sub>-TPR (D) profiles for the samples.

### 3.2. Effect of homogeneous precipitation temperature

#### 3.2.1. Structural properties

Fig. 3(A) shows the XRD patterns of samples synthesized in a water bath at 70–90 °C; the precipitation time and calcination temperature were fixed at 24 h and 500 °C, respectively. For all three samples, the diffraction peaks could be attributed to pure  $\alpha$ -MnO<sub>2</sub> (JCPDS card NO. 44–0141) [60,61], but the crystallinities were notably different. An increase in crystallinity was observed with the increase in the homogeneous precipitation temperature, as evidenced by the appearance of sharp peaks [45].

The N<sub>2</sub> isotherms and cumulative pore volume as a function of pore width of the  $\alpha$ -MnO<sub>2</sub> samples are illustrated in Fig. S9(A) and (B) respectively, which reveal their mesopore structures. The pore size distributions and the textural parameters of the  $\alpha$ -MnO<sub>2</sub> samples are presented in Fig. 3(B) and Table 2, respectively. Among them, the MnO<sub>2</sub>-90 sample had the largest BET surface area (34.30 m<sup>2</sup> g<sup>-1</sup>), followed by MnO<sub>2</sub>-80 (16.93 m<sup>2</sup> g<sup>-1</sup>) and MnO<sub>2</sub>-70 (13.82 m<sup>2</sup> g<sup>-1</sup>).

According to previous reports [62,63], this can be attributed to the gradual enhancement of the mesopore structure from 70 °C to 90 °C, as shown in Fig. S9(B).

The effect of bath temperature on  $\alpha$ -MnO<sub>2</sub> morphology was investigated by SEM and TEM as shown in Fig. 4. Well-grown nanowires (MnO<sub>2</sub>-70), nanorods (MnO<sub>2</sub>-80), and nanoparticles (MnO<sub>2</sub>-90) of  $\alpha$ -MnO<sub>2</sub> could be clearly observed. It should be noted that the wire-like morphology can be differentiated from the rod-like morphology in terms of the length. To be specific, the lengths of the wires, rods and particles were ca. 0.5–1  $\mu$ m, 65–162 nm and 20–40 nm, respectively. The HRTEM images show well-resolved lattice fringes, with spacings of 0.49 nm, 0.31 nm and 0.24 nm, respectively, which were ascribed to the (2 0 0), (3 1 0) and (2 1 1) crystal planes of  $\alpha$ -MnO<sub>2</sub>, respectively, consistent with the XRD results.

#### 3.2.2. Surface properties

The content and chemical states of the as-prepared materials were characterized by XPS and ICP-OES, as shown in Fig. 5 and Table 2. The

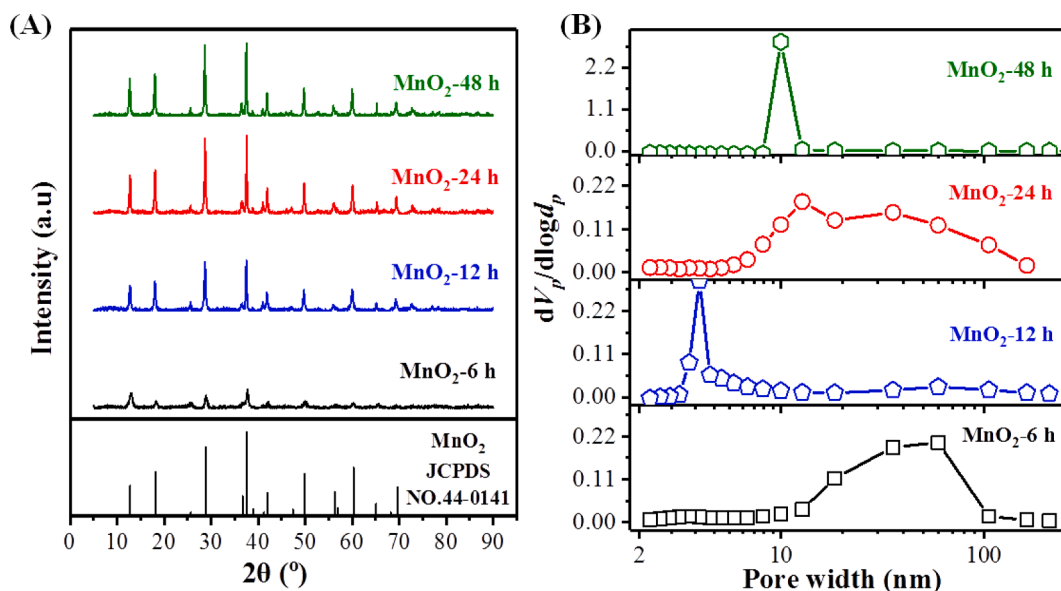


Fig. 6. Powder XRD patterns (A) and pore distributions (B) of  $\text{MnO}_2$  catalysts prepared with different bath times.

Table 3

XPS peak-fitting parameters, atomic ratios and textural parameters of  $\text{MnO}_2$  catalysts with different bath times.

Sample	Mn 2p			Mn 3 s		O 1 s			K/Mn		N <sub>2</sub> Physisorption	
	Mn <sup>3+</sup> (eV)	Mn <sup>4+</sup> (eV)	Mn <sup>4+</sup> /Mn <sup>3+</sup>	$\Delta E_s$	AOS	O <sub>latt</sub> (%)	O <sub>ads</sub> (%)	O <sub>ads</sub> /O <sub>latt</sub>	XPS	ICP	S <sub>BET</sub> (m <sup>2</sup> /g)	V <sub>n</sub> (mL/g)
MnO <sub>2</sub> -6 h	641.9	643.4	0.61	4.71	3.63	74.11	25.89	0.35	0.23	0.20	22.03	0.14
MnO <sub>2</sub> -12 h	641.8	642.9	0.97	4.65	3.70	69.25	30.75	0.44	0.19	0.15	20.54	0.05
MnO <sub>2</sub> -24 h	641.9	642.9	1.16	4.54	3.82	65.57	34.43	0.52	0.11	0.11	34.30	0.16
MnO <sub>2</sub> -48 h	641.8	642.9	1.14	4.55	3.81	66.25	33.75	0.51	0.13	0.14	36.80	0.20

asymmetrical Mn 2p 3/2 peak (Fig. 5(A)) had two components with binding energies of 641.9 and 642.9 eV, which can be ascribed to the surface Mn<sup>3+</sup> and Mn<sup>4+</sup> ions, respectively [64]. A quantitative analysis on the molar ratio of surface Mn<sup>4+</sup>/Mn<sup>3+</sup> is summarized in Table 2. It could be found that the molar ratio of surface Mn<sup>4+</sup>/Mn<sup>3+</sup> decreased in the order of MnO<sub>2</sub>-90 (1.16) > MnO<sub>2</sub>-80 (0.95) > MnO<sub>2</sub>-70 (0.90). The average oxidation state (AOS) [65] of the surface Mn ions derived from Mn 3 s was also calculated and listed in Table 2. The order of average oxidation state can be listed as follows: MnO<sub>2</sub>-90 (3.82) > MnO<sub>2</sub>-80 (3.57) > MnO<sub>2</sub>-70 (3.51), which is consistent with the Mn 2p XPS results. The amount of K plays a critical role in influencing the chemical state of Mn ions in  $\alpha$ -MnO<sub>2</sub>. The K/Mn ratios as shown in Table 2 derived from both XPS and ICP follow the order MnO<sub>2</sub>-90 < MnO<sub>2</sub>-80 < MnO<sub>2</sub>-70. Suitable preparation conditions can remove excessive K ion in the as-prepared materials. These results are consistent with many other reports [48,66] which found that decreasing the charge balance ion K is beneficial for increasing the oxidation state of skeleton Mn ions.

Surface active oxygen species were investigated from the O 1 s spectra (Fig. 5(C)), which could be deconvoluted into two peaks at 529.6 eV and around 531.1 eV, corresponding to lattice oxygen (O<sub>latt</sub>) and surface adsorbed oxygen species (O<sub>ads</sub>), respectively [67,68]. The data presented in Table 2 show that MnO<sub>2</sub>-90 possessed more abundant O<sub>ads</sub> than MnO<sub>2</sub>-80 and MnO<sub>2</sub>-70. The O<sub>ads</sub> stemmed from oxygen vacancies and had higher mobility than lattice oxygen [18,69]. Thus, this result indicates that a higher water bath temperature can effectively improve the ratio of active surface oxygen species.

The H<sub>2</sub>-TPR technique was used to study the reducibility of the three  $\alpha$ -MnO<sub>2</sub> samples, as depicted in Fig. 5(D). All of the  $\alpha$ -MnO<sub>2</sub> samples show similar overlapping reduction peaks, which is ascribed to the complete reduction of Mn<sup>4+</sup> to Mn<sup>2+</sup> [45]. The overlapping of MnO<sub>2</sub> reduction peaks is in accordance with many other reports [70–73]. The

reducibility increased with the water bath temperature and the general order was as follows: MnO<sub>2</sub>-70 < MnO<sub>2</sub>-80 < MnO<sub>2</sub>-90.

### 3.3. Effect of homogeneous precipitation time

#### 3.3.1. Structural properties

The powder XRD patterns of samples prepared with different precipitation times are exhibited in Fig. 6(A). It can be seen that increasing the bath time from 6 h to 48 h significantly enhanced the diffraction intensity, while the crystal structure of  $\alpha$ -MnO<sub>2</sub> remained intact. The degree of crystallinity generally followed the trend: MnO<sub>2</sub>-24 h  $\approx$  MnO<sub>2</sub>-48 h > MnO<sub>2</sub>-12 h > MnO<sub>2</sub>-6 h.

The N<sub>2</sub> isotherms and cumulative pore volume as a function of pore width are presented in Fig. S10(A) and (B), respectively. The BET surface areas and pore volumes are listed in Table 3. It can be observed in Fig. S10(B) that all samples exhibited a mesoporous structure. The surface areas followed the order: MnO<sub>2</sub>-48 h (36.80 m<sup>2</sup> g<sup>-1</sup>) > MnO<sub>2</sub>-24 h (34.30 m<sup>2</sup> g<sup>-1</sup>) > MnO<sub>2</sub>-6 h (22.03 m<sup>2</sup> g<sup>-1</sup>) > MnO<sub>2</sub>-12 h (20.54 m<sup>2</sup> g<sup>-1</sup>), in accordance with the enhanced mesopore structure as shown in Fig. 6(B) and Fig. S10(A). It was noted that the catalytic activity of MnO<sub>2</sub>-12 h was superior to that of MnO<sub>2</sub>-6 h, although it had smaller surface area and pore volume. This indicates that besides surface area, there are other critical factors that determine the activity of the catalyst, which will be discussed in the next section.

The evolution of morphology with precipitation time is illustrated in Fig. 7. Sample MnO<sub>2</sub>-6 h demonstrated a typical nanowire morphology. Increasing the water bath time from 6 h to 12 h resulted in the nanostructure of MnO<sub>2</sub>-12 h converting into stacked nanoparticles. Further increasing the bath time to 24 h led to a better morphology since the nanoparticles became loose and evenly distributed. The morphology of MnO<sub>2</sub>-48 h was similar to that of MnO<sub>2</sub>-24 h. The HRTEM images reveal

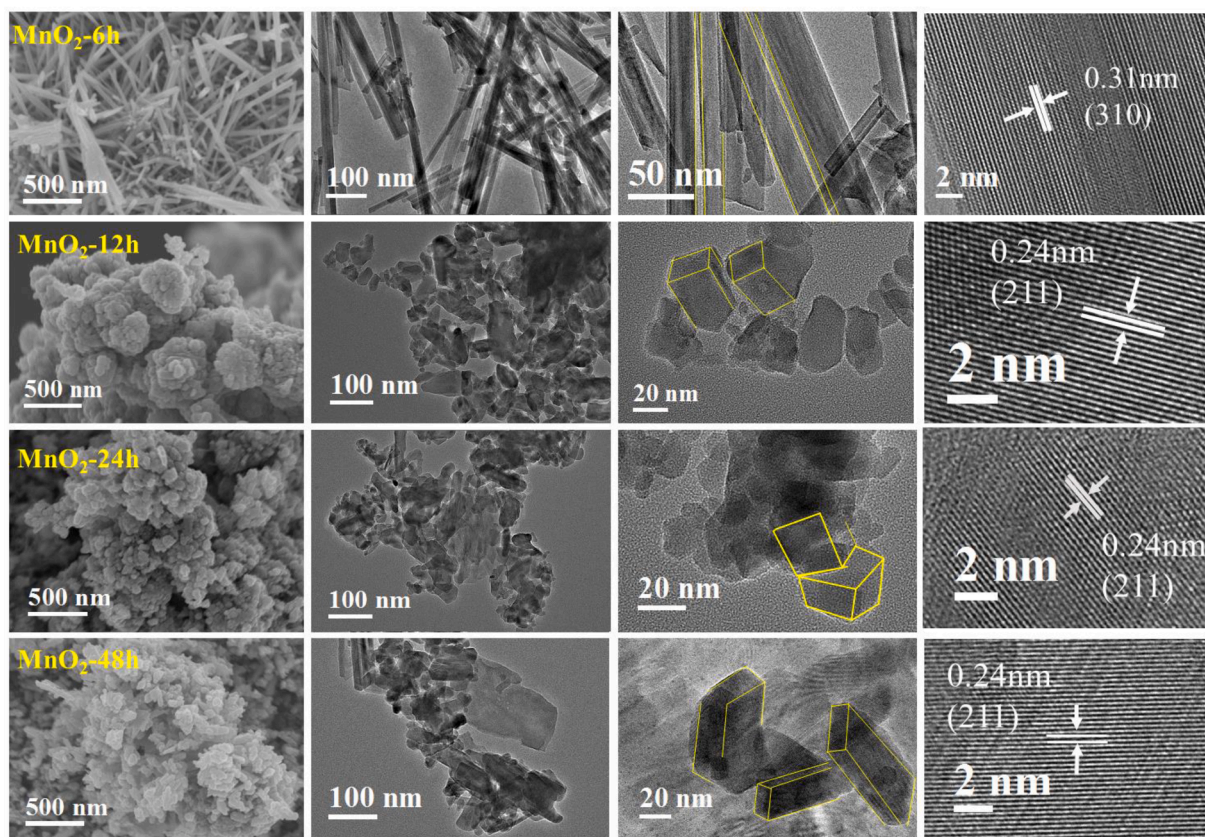


Fig. 7. Images showing the morphology of  $\text{MnO}_2$  catalysts prepared with different bath times.

that the exposed facet of  $\text{MnO}_2$ -6 h can be identified as the (3 1 0) crystal plane based on the lattice spacing of 0.31 nm, while the dominant exposed facet for all the other samples was the (2 1 1) plane, with the lattice fringe spacing of 0.24 nm.

### 3.3.2. Surface properties

The Mn 2p, Mn 3 s and O 1 s XPS spectra of  $\text{MnO}_2$  catalysts prepared with different precipitation times (the fixed precipitation and calcination temperatures were 90 °C and 500 °C respectively) are illustrated in Fig. 8 and the curve-fitting results are presented in Table 3. It was found that the surface  $\text{Mn}^{4+}/\text{Mn}^{3+}$  molar ratio decreased in the order  $\text{MnO}_2$ -24 h  $\approx$   $\text{MnO}_2$ -48 h >  $\text{MnO}_2$ -12 h >  $\text{MnO}_2$ -6 h. The AOS values of Mn followed the same sequence as the  $\text{Mn}^{4+}/\text{Mn}^{3+}$  ratio, suggesting that there were more  $\text{Mn}^{4+}$  cations on the surface of  $\text{MnO}_2$ -24 h than on other samples. As shown in Table 3, on prolonging the precipitation time from 6 h to 24 h, the K content in the crystal was decreased. The presence of excess K ion decreased the oxidation state of Mn, which is detrimental to VOC oxidation. The  $\text{O}_{\text{ads}}/\text{O}_{\text{latt}}$  molar ratios listed in Table 3 follow the order  $\text{MnO}_2$ -24 h  $\approx$   $\text{MnO}_2$ -48 h >  $\text{MnO}_2$ -12 h >  $\text{MnO}_2$ -6 h, which is consistent with the activity of the catalysts, indicating that  $\text{O}_{\text{ads}}$  played an important role in the oxidation of ethyl acetate.

The reducibility as measured by  $\text{H}_2$ -TPR is illustrated in Fig. 8. Since  $\text{MnO}_2$ -24 h shows the lowest temperature reduction peak, it possessed the most mobile oxygen species both at the surface and in the bulk among the four catalysts. In addition, the total amount of  $\text{H}_2$  consumed for these  $\alpha$ - $\text{MnO}_2$  samples decreased in the order  $\text{MnO}_2$ -24 h  $\approx$   $\text{MnO}_2$ -48 h >  $\text{MnO}_2$ -12 h >  $\text{MnO}_2$ -6 h, which indicates that the  $\text{MnO}_2$ -24 h sample possessed most abundant active oxygen species.

### 3.4. Correlation of physicochemical properties and activity

The selected  $\alpha$ - $\text{MnO}_2$  catalysts exhibited the best performance in the

total oxidation of ethyl acetate compared to all previously reported catalysts in the literature. According to the results of XRD, BET, SEM, TEM and XPS, it was found that the preparation parameters (water bath temperature and time) had remarkable influence on the properties of the  $\alpha$ - $\text{MnO}_2$  catalysts.

Increasing the bath temperature and time significantly enhanced the diffraction intensity of  $\alpha$ - $\text{MnO}_2$ , as illustrated in Fig. 3(A) and Fig. 6(A). It has been reported that sufficiently high crystallinity could lead to excellent mechanical strength and stability [74,75]. Therefore, we believe that the high crystallinity of our catalyst derived from suitable preparation conditions contributed to the superior catalytic stability of  $\alpha$ - $\text{MnO}_2$  as shown in Fig. 2. With regard to the morphology, the evolution from nanowires to nanorods and nanoparticles originating from adjusting the homogeneous precipitation conditions could lead to a substantial increase in specific surface area ( $S_{\text{BET}}$ ) (Figs. 4 and 7). Larger  $S_{\text{BET}}$  favors the catalytic performance of a material [19] due to efficient diffusion and adsorption of the reactants [76]. However, surface area was not the key factor influencing the VOC oxidation activity, since the surface area of  $\text{MnO}_2$ -12 h is smaller than that of  $\text{MnO}_2$ -6 h as listed in Table 3, whereas the VOC removal rate of  $\text{MnO}_2$ -12 h is much better than that of  $\text{MnO}_2$ -6 h, as testified in Fig. 1. The crystal plane and surface atomic configurations may play crucial roles in VOC oxidation.

VOC oxidation reactions over  $\text{MnO}_x$  catalysts generally occur by the Mars-van Krevelen mechanism [77], in which the reaction and replenishment of surface oxygen species is critical; the ethyl acetate reaction over  $\text{MnO}_2$  is analyzed in more detail in Text S4 and Fig. S11. Low-temperature reducibility is one of the key indicators for oxidation, because better reducibility indicates that surface oxygen has stronger mobility, so that more oxygen species can participate in the reaction [78]. The results of activity measurements,  $\text{H}_2$ -TPR and XPS results showed that the  $\alpha$ - $\text{MnO}_2$  catalysts with better activity exhibited better low-temperature reducibility and abundant adsorbed oxygen species, as

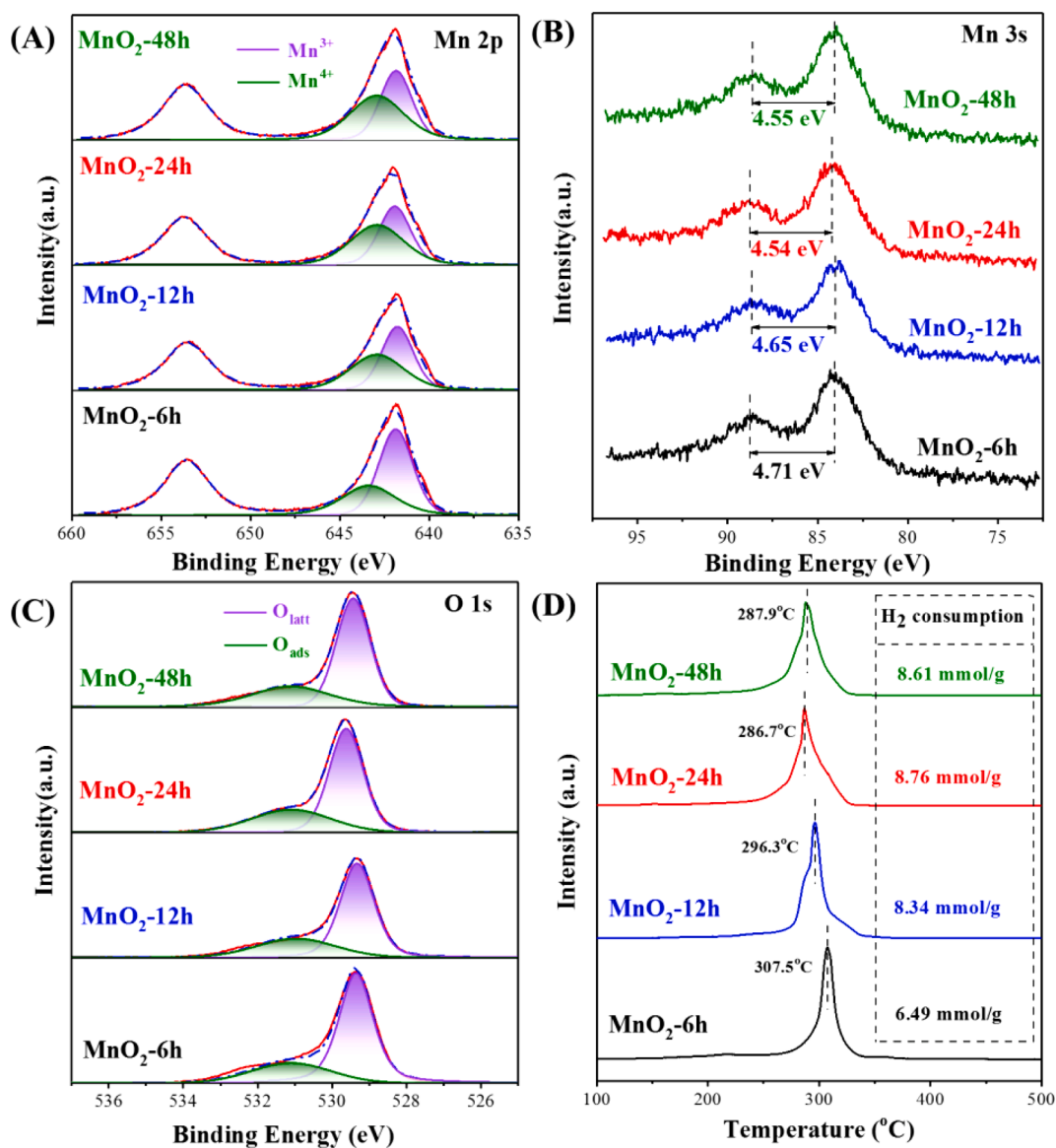


Fig. 8. XPS spectra of Mn 2p (A), Mn 3s (B), O 1s (C) and H<sub>2</sub>-TPR profiles (D) of MnO<sub>2</sub> catalysts prepared with different bath times.

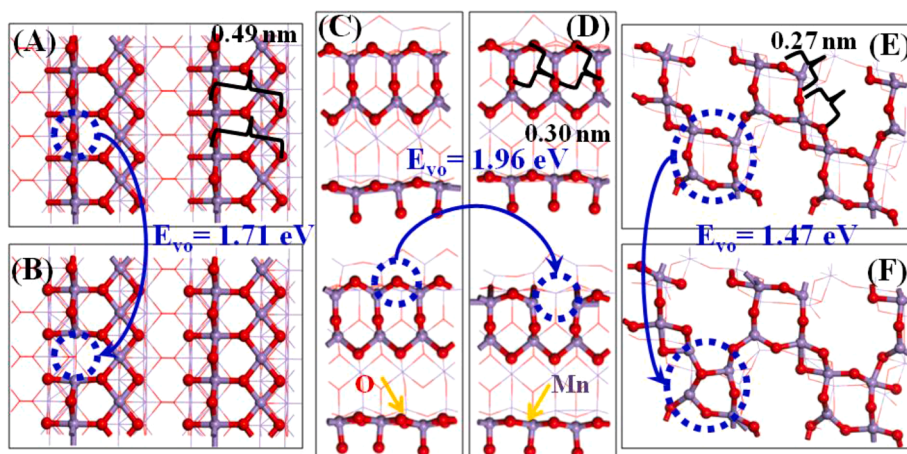


Fig. 9. Optimized models for different surfaces of  $\alpha$ -MnO<sub>2</sub>: (2 0 0) surface (A), (2 0 0) surface with oxygen vacancy (B), (3 1 0) surface (C), (3 1 0) surface with oxygen vacancy (D), (2 1 1) surface (E), and (2 1 1) surface with oxygen vacancy (F).

shown in Fig. S12. In brief, the nanoparticle sample performed better than the nanorod and nanowire samples in VOC oxidation due to the active surface oxygen species.

As stated above, surface oxygen species govern VOC oxidation, and different exposed crystal planes may have different oxygen species. With increased precipitation temperature and time, the predominant exposed surfaces of (2 0 0) and (3 1 0) evolved into the (2 1 1) surface of  $\alpha$ -MnO<sub>2</sub>, as shown in Figs. 4 and 7. The three dominant crystalline planes mainly differ in the Mn-O coordination number, which could influence the activity (Text S5). However, it is difficult to distinguish the activity of surface oxygen species originating from certain planes of  $\alpha$ -MnO<sub>2</sub> experimentally. Therefore, DFT calculations were carried out, and surface models were constructed as displayed in Fig. S13. The optimized surface lattice spacings of (2 0 0), (3 1 0) and (2 1 1) models were 0.49, 0.30, and 0.27 nm respectively as shown in Fig. 9, which are close to the experimental results. After the depletion of one surface oxygen atom, the atomic configurations of the (2 0 0) and (3 1 0) surfaces were almost the same as that of the corresponding pristine surface, as shown in Fig. 9(B) and (D), whereas a distinct surface re-construction took place on (2 1 1) surface as shown in Fig. 9(F). The oxygen vacancy formation energy was also calculated to reveal the reactivity of surface oxygen species, which varied as follows: (2 1 1) < (2 0 0) < (3 1 0). The (2 1 1) surface had the lowest  $E_{vo}$  value, which indicates that an oxygen vacancy can readily form on the surface and that the oxygen species are the most active, which is in accordance with the experimental results for activity. Another study also verified that the (2 1 1) facet of  $\alpha$ -MnO<sub>2</sub> is conducive to the formation of oxygen vacancies due to the presence of unsaturated manganese ions [42]. Therefore, the experimental and theoretical results were consistent with each other and confirmed that the oxygen species originating from the (2 1 1) surface are the most active in the combustion of VOCs.

#### 4. Conclusion

A urea-aided homogeneous precipitation method was successfully applied in preparing  $\alpha$ -MnO<sub>2</sub> catalysts. Different morphologies of nanowires, nanorods and nanoparticles were obtained simply by tuning the precipitation conditions. With increasing precipitation temperature and time, the evolution in morphology from nanowires to particles could be clearly observed. The main exposed surface evolved from (2 0 0), (3 1 0) to (2 1 1) eventually. The degree of crystallinity, BET surface area and amount of surface adsorbed oxygen of  $\alpha$ -MnO<sub>2</sub> also exhibited a substantial increase. The optimal precipitation temperature and time were 90 °C and 24 h respectively. The as-obtained MnO<sub>2</sub> catalyst exhibited excellent activity and stability in the oxidation of ethyl acetate. The  $T_{50}$  and  $T_{90}$  values were 150 °C and 176 °C respectively. In a 113-h long test, the catalyst could maintain 100% ethyl acetate conversion and nearly 100% CO<sub>2</sub> yield at a temperature of 190 °C, which is far better than the performance of a commercial Pd-based catalyst. With the aid of experimental characterization and DFT calculation, oxygen species originating from different surfaces were compared, among which the surface oxygen from the (2 1 1) surface was found to be most active. This study provides a facile way to manipulate the exposed surfaces of MnO<sub>2</sub> to enhance VOC oxidation.

#### Declaration of Competing Interest

The authors declare that they have no known competing financial interests or personal relationships that could have appeared to influence the work reported in this paper.

#### Acknowledgements

The work was supported by the National Key R&D Program of China (2017YFE0127500), the Youth Innovation Promotion Association, Chinese Academy of Sciences (2019306), the National Natural Science

Foundation of China (21936005) and the Science and Technology Planning Project of Xiamen City (NO. 3502Z20191021).

#### Appendix A. Supplementary data

Supplementary data to this article can be found online at <https://doi.org/10.1016/j.cej.2021.129246>.

#### References

- [1] Q. Zhao, Y. Li, X. Chai, L. Xu, L. Zhang, P. Ning, J. Huang, S. Tian, Interaction of inhalable volatile organic compounds and pulmonary surfactant: Potential hazards of VOCs exposure to lung, *J. Hazard. Mater.* 369 (2019) 512–520, <https://doi.org/10.1016/j.jhazmat.2019.01.104>.
- [2] M.S. Kamal, S.A. Razzak, M.M. Hossain, Catalytic oxidation of volatile organic compounds (VOCs) – A review, *Atmos. Environ.* 140 (2016) 117–134, <https://doi.org/10.1016/j.atmosenv.2016.05.031>.
- [3] C. He, J. Cheng, X. Zhang, M. Douthwaite, S. Pattison, Z. Hao, Recent advances in the catalytic oxidation of volatile organic compounds: A review based on pollutant sorts and sources, *Chem. Rev.* 119 (2019) 4471–4568, <https://doi.org/10.1021/acs.chemrev.8b00408>.
- [4] M. Li, Q. Zhang, B. Zheng, D. Tong, Y. Lei, F. Liu, C. Hong, S. Kang, L. Yan, Y. Zhang, Y. Bo, H. Su, Y. Cheng, K. He, Persistent growth of anthropogenic non-methane volatile organic compound (NMVOC) emissions in China during 1990–2017: drivers, speciation and ozone formation potential, *Atmos. Chem. Phys.* 19 (2019) 8897–8913, <https://doi.org/10.5194/acp-19-8897-2019>.
- [5] Y. Xia, et al., Concurrent catalytic removal of typical volatile organic compound mixtures over Au-Pd/alpha-MnO<sub>2</sub> nanotubes, *J. Environ. Sci. (China)* 64 (2018) 276–288, <https://doi.org/10.1016/j.jes.2017.06.025>.
- [6] P. Papaefthimiou, T. Ioannides, X.E. Verykios, VOC removal: Investigation of ethylacetate oxidation over supported Pt catalysts, *Catal. Today* 54 (1999) 81–92, [https://doi.org/10.1016/S0920-5861\(99\)00170-4](https://doi.org/10.1016/S0920-5861(99)00170-4).
- [7] X. Wang, TiO<sub>2</sub> and ZrO<sub>2</sub> crystals in SBA-15 silica: performance of Pt/TiO<sub>2</sub>(ZrO<sub>2</sub>)/SBA-15 catalysts in ethyl acetate combustion, *J. Catal.* 222 (2004) 565–571, <https://doi.org/10.1016/j.jcat.2003.12.003>.
- [8] Y. Ma, M. Chen, C. Song, X. Zheng, Catalytic oxidation of toluene, acetone and ethyl acetate on a new Pt-Pd/stainless steel wire mesh catalyst, *Acta Phys.-Chim. Sin.* 24 (2008) 1132–1136, [https://doi.org/10.1016/S1872-1508\(08\)60047-9](https://doi.org/10.1016/S1872-1508(08)60047-9).
- [9] Y.F. Wang, C.B. Zhang, F.D. Liu, H. He, Well-dispersed palladium supported on ordered mesoporous Co<sub>3</sub>O<sub>4</sub> for catalytic oxidation of o-xylene, *Appl. Catal. B* 142 (2013) 72–79, <https://doi.org/10.1016/j.apcatb.2013.05.003>.
- [10] W. Pei, Y. Liu, J. Deng, K. Zhang, Z. Hou, X. Zhao, H. Dai, Partially embedding Pt nanoparticles in the skeleton of 3DOM Mn<sub>2</sub>O<sub>3</sub>: An effective strategy for enhancing catalytic stability in toluene combustion, *Appl. Catal. B* 256 (2019), 117814, <https://doi.org/10.1016/j.apcatb.2019.117814>.
- [11] S.Y. Huang, C.B. Zhang, H. He, Effect of pretreatment on Pd/Al<sub>2</sub>O<sub>3</sub> catalyst for catalytic oxidation of o-xylene at low temperature, *J. Environ. Sci.* 25 (2013) 1206–1212, [https://doi.org/10.1016/S1001-0742\(12\)60169-7](https://doi.org/10.1016/S1001-0742(12)60169-7).
- [12] L. Yosefi, M. Haghghi, S. Allahyari, Abatement of toluene from polluted air over Mn/Clinoptilolite-CeO<sub>2</sub> nanopowder: Impregnation vs. ultrasound assisted synthesis with various Mn-loading, *Adv. Powder Technol.* 26 (2015) 602–611, <https://doi.org/10.1016/j.appt.2015.01.009>.
- [13] H. Wang, Z. Huang, Z. Jiang, Trifunctional C@MnO catalyst for enhanced stable simultaneously catalytic removal of formaldehyde and ozone, *ACS Catal.* 8 (2016) 3164–3180, <https://doi.org/10.1021/acscatal.8b00309>.
- [14] S. Li, Q. Hao, R. Zhao, D. Liu, H. Duan, B. Dou, Highly efficient catalytic removal of ethyl acetate over Ce/Zr promoted copper/ZSM-5 catalysts, *Chem. Eng. J.* 285 (2016) 536–543, <https://doi.org/10.1016/j.cej.2015.09.097>.
- [15] P. Yang, S. Yang, Z. Shi, Z. Meng, R. Zhou, Deep oxidation of chlorinated VOCs over CeO<sub>2</sub>-based transition metal mixed oxide catalysts, *Appl. Catal., B* 162 (2015) 227–235, <https://doi.org/10.1016/j.apcatb.2014.06.048>.
- [16] L. Li, et al., Facile synthesis  $\lambda$ -MnO<sub>2</sub> spinel for highly effective catalytic oxidation of benzene, *Chem. Eng. J.* (2020), <https://doi.org/10.1016/j.cej.2020.127828>.
- [17] C. Dong, et al., Revealing the highly catalytic performance of spinel CoMn<sub>2</sub>O<sub>4</sub> for toluene oxidation: Involvement and replenishment of oxygen species using in situ Designed-TP techniques, *ACS Catal.* 9 (8) (2019) 6698–6710, <https://doi.org/10.1021/acscatal.9b01324>.
- [18] S.C. Kim, W.G. Shim, Catalytic combustion of VOCs over a series of manganese oxide catalysts, *Appl. Catal. B* 98 (2010) 180–185, <https://doi.org/10.1016/j.apcatb.2010.05.027>.
- [19] W. Si, Y. Wang, Y. Peng, X. Li, K. Li, J. Li, A high-efficiency gamma-MnO<sub>2</sub>-like catalyst in toluene combustion, *Chem. Commun. (Camb)* 51 (2015) 14977–14980, <https://doi.org/10.1039/c5cc04528b>.
- [20] Y. Jiang, J. Gao, Q. Zhang, Z. Liu, M. Fu, J. Wu, Y. Hu, D. Ye, Enhanced oxygen vacancies to improve ethyl acetate oxidation over MnO<sub>x</sub>-CeO<sub>2</sub> catalyst derived from MOF template, *Chem. Eng. J.* 371 (2019) 78–87, <https://doi.org/10.1016/j.cej.2019.03.233>.
- [21] X. Zeng, B. Li, R. Liu, X. Li, T. Zhu, Investigation of promotion effect of Cu doped MnO<sub>2</sub> catalysts on ketone-type VOCs degradation in a one-stage plasma-catalysis system, *Chem. Eng. J.* 384 (2020), <https://doi.org/10.1016/j.cej.2019.123362>.
- [22] Y. Xu, J. Dhainaut, G. Rochard, J.-P. Dacquin, A.-S. Mamede, J.-M. Giraudon, J.-F. Lamonier, H. Zhang, S. Royer, Hierarchical porous epsilon-MnO<sub>2</sub> from

- perovskite precursor: Application to the formaldehyde total oxidation, *Chem. Eng. J.* 388 (2020), <https://doi.org/10.1016/j.cej.2020.124146>.
- [23] Z.G. Zhou, H.M. Du, Z.H. Dai, Y. Mu, L.L. Tong, Q.J. Xing, S.S. Liu, Z.M. Ao, J. P. Zou, Degradation of organic pollutants by peroxymonosulfate activated by MnO<sub>2</sub> with different crystalline structures: Catalytic performances and mechanisms, *Chem. Eng. J.* 374 (2019) 170–180, <https://doi.org/10.1016/j.cej.2019.05.170>.
- [24] D.F.M. Santos, O.S.G.P. Soares, J.L. Figueiredo, O. Sanz, M. Montes, M.F.R. Pereira, Preparation of ceramic and metallic monoliths coated with cryptomelane as catalysts for VOC abatement, *Chem. Eng. J.* 382 (2020), <https://doi.org/10.1016/j.cej.2019.122923>.
- [25] M. Sun, L. Yu, F. Ye, G. Diao, Q. Yu, Z. Hao, Y. Zheng, L. Yuan, Transition metal doped cryptomelane-type manganese oxide for low-temperature catalytic combustion of dimethyl ether, *Chem. Eng. J.* 220 (2013) 320–327, <https://doi.org/10.1016/j.cej.2013.01.061>.
- [26] B. Chen, B. Wu, L. Yu, M. Crocker, C. Shi, Investigation into the catalytic roles of various oxygen species over different crystal phases of MnO<sub>2</sub> for C<sub>6</sub>H<sub>6</sub> and HCHO oxidation, *ACS Catal.* 10 (2020) 6176–6187, <https://doi.org/10.1021/acscatal.0c00459>.
- [27] Y. Dong, J. Zhao, J.-Y. Zhang, Y. Chen, X. Yang, W. Song, L. Wei, W. Li, Synergy of Mn and Ni enhanced catalytic performance for toluene combustion over Ni-doped alpha-MnO<sub>2</sub> catalysts, *Chem. Eng. J.* 388 (2020), <https://doi.org/10.1016/j.cej.2020.124244>.
- [28] J. Li, Z. Qu, Y. Qin, H. Wang, Effect of MnO<sub>2</sub> morphology on the catalytic oxidation of toluene over Ag/MnO<sub>2</sub> catalysts, *Appl. Surf. Sci.* 385 (2016) 234–240, <https://doi.org/10.1016/j.apsusc.2016.05.114>.
- [29] S.K. Meher, G.R. Rao, Morphology-controlled promoting activity of nanostructured MnO<sub>2</sub> for methanol and ethanol electrooxidation on Pt/C, *J. Phys. Chem. C* 117 (2013) 4888–4900, <https://doi.org/10.1021/jp3093995>.
- [30] W. Xiao, D.L. Wang, X.W. Lou, Shape-controlled synthesis of MnO<sub>2</sub> nanostructures with enhanced electrocatalytic activity for oxygen reduction, *J. Phys. Chem. C* 114 (2010) 1694–1700, <https://doi.org/10.1021/jp909386d>.
- [31] F. Wang, H. Dai, J. Deng, G. Bai, K. Ji, Y. Liu, Manganese oxides with rod-, wire-, tube-, and flower-like morphologies: highly effective catalysts for the removal of toluene, *Environ. Sci. Technol.* 46 (2012) 4034–4041, <https://doi.org/10.1021/es204038j>.
- [32] F. Hashemzadeh, M. Mehdi Kashani Motlagh, A. Maghsoudipour, A comparative study of hydrothermal and sol-gel methods in the synthesis of MnO<sub>2</sub> nanostructures, *J. Sol-Gel Sci. Technol.* 51 (2009) 169–174, <https://doi.org/10.1007/s10971-009-1978-2>.
- [33] J. Livage, Sol-gel synthesis of heterogeneous catalysts from aqueous solutions, *Catal. Today* 41 (1998) 3–19, [https://doi.org/10.1016/S0920-5861\(98\)00034-0](https://doi.org/10.1016/S0920-5861(98)00034-0).
- [34] M.R. Morales, B.P. Barbero, L.E. Cadús, Combustion of volatile organic compounds on manganese iron or nickel mixed oxide catalysts, *Appl. Catal., B* 74 (2007) 1–10, <https://doi.org/10.1016/j.apcatb.2007.01.008>.
- [35] J. Chen, X. Chen, X. Chen, W.J. Xu, Z. Xu, H.P. Jia, J. Chen, Homogeneous introduction of CeO<sub>2</sub> into MnOx-based catalyst for oxidation of aromatic VOCs, *Appl. Catal. B* 224 (2018) 825–835, <https://doi.org/10.1016/j.apcatb.2017.11.036>.
- [36] N. Zhang, L. Li, Y. Guo, J. He, R. Wu, L. Song, G. Zhang, J. Zhao, D. Wang, H. He, A MnO<sub>2</sub>-based catalyst with H<sub>2</sub>O resistance for NH<sub>3</sub>-SCR: Study of catalytic activity and reactants-H<sub>2</sub>O competitive adsorption, *Appl. Catal. B* 270 (2020), <https://doi.org/10.1016/j.apcatb.2020.118860>.
- [37] W. Shan, F. Liu, H. He, X. Shi, C. Zhang, Novel cerium-tungsten mixed oxide catalyst for the selective catalytic reduction of NO<sub>x</sub> with NH<sub>3</sub>, *Chem Commun (Camb)* 47 (2011) 8046–8048, <https://doi.org/10.1039/c1cc12168e>.
- [38] F. Schurz, et al., Octahedral molecular sieves of the type K-OMS-2 with different particle sizes and morphologies: Impact on the catalytic properties in the aerobic partial oxidation of benzyl alcohol, *Appl. Catal. A: General* 355 (1–2) (2009) 42–49.
- [39] X. Wang, Y. Li, Rational synthesis of alpha-MnO<sub>2</sub> single-crystal nanorods, *Chem. Commun. (Camb)* 7 (2002) 764–765, <https://doi.org/10.1016/j.apcata.2008.11.014>.
- [40] H.M. Galindo, et al., Facile one-step template-free synthesis of uniform hollow microstructures of cryptomelane-type manganese oxide K-OMS-2, *Langmuir* 26 (16) (2010) 13677–13683, <https://doi.org/10.1021/la102404j>.
- [41] Y. Wang, et al., Crystallization behavior of 3D-structured OMS-2 under hydrothermal conditions, *CrystEngComm* 17 (19) (2015) 3636–3644, <https://doi.org/10.1039/C5CE00278H>.
- [42] J. Jia, P. Zhang, L. Chen, The effect of morphology of alpha-MnO<sub>2</sub> on catalytic decomposition of gaseous ozone, *Catal. Sci. Technol.* 6 (2016) 5841–5847, <https://doi.org/10.1039/c6cy00301j>.
- [43] J. Hou, et al., Effect of giant oxygen vacancy defects on the catalytic oxidation of OMS-2 nanorods, *J. Mater. Chem. A* 1 (23) (2013), <https://doi.org/10.1039/C3TA11566F>.
- [44] F. Wang, et al., Unraveling the effects of the coordination number of Mn over alpha-MnO<sub>2</sub> catalysts for toluene oxidation, *Chem. Eng. J.* 396 (2020) 13, <https://doi.org/10.1016/j.cej.2020.125192>.
- [45] S. Rong, P. Zhang, F. Liu, Y. Yang, Engineering crystal facet of alpha-MnO<sub>2</sub> nanowire for highly efficient catalytic oxidation of carcinogenic airborne formaldehyde, *ACS Catal.* 8 (2018) 3435–3446, <https://doi.org/10.1021/acscatal.8b00456>.
- [46] K. Yang, G. Mul, J. Choi, J. Mouljin, J. Chung, Development of TiO<sub>2</sub>/Ti wire-mesh honeycomb for catalytic combustion of ethyl acetate in air, *Appl. Catal. A* 313 (2006) 86–93, <https://doi.org/10.1016/j.apcata.2006.07.008>.
- [47] S. Chen, S.-H. Yu, B. Yu, L. Ren, W. Yao, H. Cölfen, Solvent effect on mineral modification: Selective synthesis of cerium compounds by a facile solution route, *Chem. - Eur. J.* 10 (2004) 3050–3058, <https://doi.org/10.1002/chem.200306066>.
- [48] J. Hou, et al., Tuning the K<sup>+</sup> concentration in the tunnel of OMS-2 Nanorods leads to a significant enhancement of the catalytic activity for benzene oxidation, *Environ. Sci. Technol.* 47 (23) (2013) 13730–13736, <https://doi.org/10.1021/ea403910s>.
- [49] G. Zhu, J. Zhu, W. Li, W. Yao, R. Zong, Y. Zhu, Q. Zhang, Tuning the K<sup>+</sup> concentration in the tunnels of alpha-MnO<sub>2</sub> to increase the content of oxygen vacancy for ozone elimination, *Environ. Sci. Technol.* 52 (2018) 8684–8692, <https://doi.org/10.1021/acs.est.8b01594>.
- [50] W. Hong, T. Zhu, Y. Sun, H. Wang, X. Li, F. Shen, Enhancing oxygen vacancies by introducing Na<sup>+</sup> into OMS-2 tunnels to promote catalytic ozone decomposition, *Environ. Sci. Technol.* 53 (2019) 13332–13343, <https://doi.org/10.1021/acs.est.9b03689>.
- [51] M. Sun, W. Li, B. Zhang, G. Cheng, B. Lan, F. Ye, Y. Zheng, X. Cheng, L. Yu, Enhanced catalytic performance by oxygen vacancy and active interface originated from facile reduction of OMS-2, *Chem. Eng. J.* 331 (2018) 626–635, <https://doi.org/10.1016/j.cej.2017.09.028>.
- [52] T. Tsoncheva, R. Ivanova, M. Dimitrov, D. Paneva, D. Kovacheva, J. Henych, P. Vomacka, M. Kormunda, N. Velinov, I. Mitov, V. Stengl, Template-assisted hydrothermally synthesized iron-titanium binary oxides and their application as catalysts for ethyl acetate oxidation, *Appl. Catal. A* 528 (2016) 24–35, <https://doi.org/10.1016/j.apcata.2016.09.006>.
- [53] M. Konsolakis, S.A.C. Carabineiro, G.E. Marnellos, M.F. Asad, O. Soares, M.F. R. Pereira, J.J.M. Orfao, J.L. Figueiredo, Effect of cobalt loading on the solid state properties and ethyl acetate oxidation performance of cobalt-cerium mixed oxides, *J. Colloid Interface Sci.* 496 (2017) 141–149, <https://doi.org/10.1016/j.jcis.2017.02.014>.
- [54] T. Tsoncheva, G. Issa, T. Blasco, P. Concepcion, M. Dimitrov, S. Hernandez, D. Kovacheva, G. Atanasova, J.M. Lopez Nieto, Silica supported copper and cerium oxide catalysts for ethyl acetate oxidation, *J. Colloid Interface Sci.* 404 (2013) 155–160, <https://doi.org/10.1016/j.jcis.2013.05.005>.
- [55] Y. Zhou, H. Zhang, Y. Yan, Catalytic oxidation of ethyl acetate over CuO/ZSM-5 catalysts: Effect of preparation method, *J. Taiwan Inst. Chem. Eng.* 84 (2018) 162–172, <https://doi.org/10.1016/j.jtice.2018.01.016>.
- [56] T. Pei, L. Liu, L. Xu, Y. Li, D. He, A novel glass fiber catalyst for the catalytic combustion of ethyl acetate, *Catal. Commun.* 74 (2016) 19–23, <https://doi.org/10.1016/j.catcom.2015.10.030>.
- [57] K.S. Yang, J.S. Choi, J.S. Chung, Evaluation of wire-mesh honeycomb containing porous Al/Al<sub>2</sub>O<sub>3</sub> layer for catalytic combustion of ethyl acetate in air, *Catal. Today* 97 (2004) 159–165, <https://doi.org/10.1016/j.cattod.2004.04.057>.
- [58] X.-W. Su, L.-Y. Jin, J.-Q. Lu, M.-F. Luo, Pd/Ce<sub>0.9</sub>Cu<sub>0.1</sub>O<sub>1.9</sub>Y<sub>2</sub>O<sub>3</sub> catalysts for catalytic combustion of toluene and ethyl acetate, *J. Ind. Eng. Chem.* 15 (2009) 683–686, <https://doi.org/10.1016/j.jiec.2009.09.045>.
- [59] S. Kang, et al., Significant enhancement in water resistance of Pd/Al<sub>2</sub>O<sub>3</sub> catalyst for benzene oxidation by Na addition, *Chinese Chem. Lett.* 30 (7) (2019) 1450–1454, <https://doi.org/10.1016/j.ccl.2019.03.023>.
- [60] M.R. Majidi, F. Shahbazi Farahani, M. Hosseini, I. Ahadzadeh, Low-cost nanowired alpha-MnO<sub>2</sub>/C as an ORR catalyst in air-cathode microbial fuel cell, *Bioelectrochemistry* 125 (2019) 38–45, <https://doi.org/10.1016/j.bioelechem.2018.09.004>.
- [61] W. Ma, S. Chen, S. Yang, W. Chen, Y. Cheng, Y. Guo, S. Peng, S. Ramakrishna, M. Zhu, Hierarchical MnO<sub>2</sub> nanowire/graphene hybrid fibers with excellent electrochemical performance for flexible solid-state supercapacitors, *J. Power Sources* 306 (2016) 481–488, <https://doi.org/10.1016/j.jpowsour.2015.12.063>.
- [62] H. Deng, S. Kang, J. Ma, C. Zhang, H. He, Silver incorporated into cryptomelane-type manganese oxide boosts the catalytic oxidation of benzene, *Appl. Catal. B* 239 (2018) 214–222, <https://doi.org/10.1016/j.apcatb.2018.08.006>.
- [63] H. Deng, S. Kang, J. Ma, L. Wang, C. Zhang, H. He, Role of structural defects in MnOx promoted by Ag doping in the catalytic combustion of volatile organic compounds and ambient decomposition of O<sub>3</sub>, *Environ. Sci. Technol.* 53 (2019) 10871–10879, <https://doi.org/10.1021/acs.est.9b01822>.
- [64] X. Zhang, Y. Junhui, Y. Jing, C. Ting, X. Bei, L. Zhe, Z. Kunfeng, Y. Ling, H. Dannong, Excellent low-temperature catalytic performance of nanosheet Co-Mn oxides for total benzene oxidation, *Appl. Catal. A* 566 (2018) 104–112, <https://doi.org/10.1016/j.apcata.2018.05.039>.
- [65] V.P. Santos, M.F.R. Pereira, J.J.M. Orfao, J.L. Figueiredo, Synthesis and characterization of manganese oxide catalysts for the total oxidation of ethyl acetate, *Top. Catal.* 52 (2009) 470–481, <https://doi.org/10.1007/s11244-009-9187-3>.
- [66] J. Wang, et al., Understanding the “seesaw effect” of interlayered K<sup>+</sup> with different structure in manganese oxides for the enhanced formaldehyde oxidation, *Appl. Catal. B: Environ.* 224 (2018) 863–870, <https://doi.org/10.1016/j.apcatb.2017.11.019>.
- [67] Y. Li, C. Zhang, J. Ma, M. Chen, H. Deng, H. He, High temperature reduction dramatically promotes Pd/TiO<sub>2</sub> catalyst for ambient formaldehyde oxidation, *Appl. Catal., B* 217 (2017) 560–569, <https://doi.org/10.1016/j.apcatb.2017.06.023>.
- [68] B. Bai, J. Li, J. Hao, 1D-MnO<sub>2</sub>, 2D-MnO<sub>2</sub> and 3D-MnO<sub>2</sub> for low-temperature oxidation of ethanol, *Appl. Catal., B* 164 (2015) 241–250, <https://doi.org/10.1016/j.apcatb.2014.08.044>.
- [69] H. Pan, Y. Jian, C. Chen, C. He, Z. Hao, Z. Shen, H. Liu, Sphere-shaped Mn<sub>3</sub>O<sub>4</sub> catalyst with remarkable low-temperature activity for methyl-ethyl-ketone combustion, *Environ. Sci. Technol.* 51 (2017) 6288–6297, <https://doi.org/10.1021/acs.est.7b00136>.
- [70] B. He, G. Cheng, S. Zhao, X. Zeng, Y. Li, R. Yang, M. Sun, L. Yu, Controlled synthesis of tunnel-structured MnO<sub>2</sub> through hydrothermal transformation of delta-MnO<sub>2</sub> and their catalytic combustion of dimethyl ether, *J. Solid State Chem.* 269 (2019) 305–311, <https://doi.org/10.1016/j.jssc.2018.09.005>.

- [71] Y. Yang, J. Jia, Y. Liu, P. Zhang, The effect of tungsten doping on the catalytic activity of  $\alpha$ -MnO<sub>2</sub> nanomaterial for ozone decomposition under humid condition, *Appl. Catal., A* 562 (2018) 132–141, <https://doi.org/10.1016/j.apcata.2018.06.006>.
- [72] G. Cheng, L. Yu, B. He, M. Sun, B. Zhang, W. Ye, B. Lan, Catalytic combustion of dimethyl ether over  $\alpha$ -MnO<sub>2</sub> nanostructures with different morphologies, *Appl. Surf. Sci.* 409 (2017) 223–231, <https://doi.org/10.1016/j.apsusc.2017.02.218>.
- [73] J. Zhang, Y. Li, L. Wang, C. Zhang, H. He, Catalytic oxidation of formaldehyde over manganese oxides with different crystal structures, *Catal. Sci. Technol.* 5 (2015) 2305–2313, <https://doi.org/10.1039/c4cy01461h>.
- [74] Y. Sim, I. Yang, D. Kwon, J.-M. Ha, J.C. Jung, Preparation of LaAlO<sub>3</sub> perovskite catalysts by simple solid-state method for oxidative coupling of methane, *Catal. Today* 352 (2020) 134–139, <https://doi.org/10.1016/j.cattod.2019.10.038>.
- [75] J. Zhu, W. Zhang, Q. Qi, H. Zhang, Y. Zhang, D. Sun, P. Liang, Catalytic oxidation of toluene, ethyl acetate and chlorobenzene over Ag/MnO<sub>2</sub>-cordierite molded catalyst, *Sci. Rep.* 9 (2019), <https://doi.org/10.1038/s41598-019-48506-5>.
- [76] J. Wang, G. Zhang, P. Zhang, Layered birnessite-type MnO<sub>2</sub> with surface pits for enhanced catalytic formaldehyde oxidation activity, *J. Mater. Chem. A* 5 (2017) 5719–5725, <https://doi.org/10.1039/c6ta09793f>.
- [77] Y. Chen, Z. Huang, M. Zhou, Z. Ma, J. Chen, X. Tang, Single silver adatoms on nanostructured manganese oxide surfaces: Boosting oxygen activation for benzene abatement, *Environ. Sci. Technol.* 51 (2017) 2304–2311, <https://doi.org/10.1021/acs.est.6b04340>.
- [78] Y. Xia, H. Dai, H. Jiang, L. Zhang, J. Deng, Y. Liu, Three-dimensionally ordered and wormhole-like mesoporous iron oxide catalysts highly active for the oxidation of acetone and methanol, *J. Hazard. Mater.* 186 (2011) 84–91, <https://doi.org/10.1016/j.jhazmat.2010.10.073>.